Hydrogen storage in high-entropy alloys with varying degree of local lattice strain

Magnus Moe Nygård[a,*], Gustav Ek[b], Dennis Karlsson[b], Martin Sahlberg[b],
Magnus H. Sørby[a], Bjørn C. Hauback[a]

[a] *Institute for Energy Technology, Department of Neutron Materials Characterization, P.O. Box 40, NO-2027 Kjeller, Norway*
[b] *Department of Chemistry - Ångström Laboratory, Uppsala University, Box 523, SE-75120 Uppsala, Sweden*

Abstract

We have investigated the structure and hydrogenation properties of a series of Ti, V, Zr, Nb and Ta based high-entropy alloys (HEAs) with varying degree of local lattice strain by means of synchrotron radiation X-ray diffraction, scanning electron microscopy, thermogravimetric analysis, differential scanning calorimetry and manometric measurements in a Sieverts apparatus. The obtained alloys have body-centred cubic (bcc) crystal structures and form face-centred cubic (fcc) hydrides with hydrogen-to-metal ratios close to 2. No correlation between the hydrogen storage capacity and the local lattice strain δr is observed in this work. Both bcc and fcc unit cells expand linearly with the zirconium-to-metal ratio [Zr]/[M], and increased concentration of Zr stabilizes the hydrides. When heated, the hydrides decompose into the original bcc alloys if [Zr]/[M]$<$12.5 at.%. The hydrides phase-separate in a hydrogen-induced decomposition type process for [Zr]/[M]$\geq$12.5 at.%. The result is then a combination of two bcc phases, one with a larger and

---

[*] Corresponding author: magnus.moe.nygaard@ife.no

the other with a smaller unit cell than the original bcc alloy.

Keywords: metal hydrides, hydrogen storage, high-entropy alloys, HEAs

---

Introduction

High-entropy alloys (HEAs) receive attention due to their diverse and often extraordinary features such as excellent mechanical properties at extreme temperatures, superparamagnetism, a large magnetocaloric effect and superconductivity [1]. HEAs typically contain four or more principle elements in near-equimolar amounts that are randomly distributed over a single crystallographic site. Furthermore, they tend to form single-phase solid solutions with simple structures such as body-centred cubic (bcc), face-centred cubic (fcc) or hexagonal close-packed (hcp). Yang et al. have suggested that one can predict whether a HEA is able to form from the two parameters Ω and δr [2]. Ω is derived in [2] following a quasi-chemical approach and is given by

$$\Omega = \frac{T_m \Delta S_{mix}}{|\Delta H_{mix}|} \tag{1}$$

where T_m is the melting point temperature of the alloy, ΔS_{mix} is the entropy of mixing and ΔH_{mix} is the enthalpy of mixing. The δr parameter account for the atomic size mismatch of the constituent atoms within the alloy and is defined as

$$\delta r = \sqrt{\sum_{i=1}^{n} \left\{ c_i \left(1 - \frac{r_i}{\bar{r}}\right)^2 \right\}} \cdot 100\% \tag{2}$$

where $\overline{r}$ is the mean atomic radius and c_i is the atomic percentage of the i^{th} element with atomic radius r_i. Hence, δr provides an estimate of the degree of local lattice strain within the HEA. To obtain an HEA one should according to [2] have

$$\Omega \geq \Omega_c = 1.1 \tag{3}$$

$$\delta r \leq \delta r_c = 6.6\% \tag{4}$$

Hydrogen storage has been suggested as an application area for HEAs as many of the elements commonly found in the alloys [3] form binary metal hydrides [4]. In general, the development of effective hydrogen storage systems is considered as crucial for widespread use of hydrogen as an energy carrier. Metal hydrides are attractive materials for such an application as they can achieve higher volumetric hydrogen densities than even liquid H_2 [5]. Nevertheless, their applicability is often limited by low gravimetric hydrogen density, poor H_2 sorption kinetics, non-reversibility, demand of extensive activation procedures and the metal hydrides being too stable [6–8]. It is expected that the HEA-concept will allow a larger degree of tunability in the properties of the corresponding metal hydrides. However, hydrogen storage in HEAs is still in its infancy with only a few reported studies [9–19]. A particularly interesting result is that a bcc ($Im\overline{3}m$) HEA of TiVZrNbHf with $(\delta r, \Omega) = (6.08~\%, 136.87)$ was reported to absorb hydrogen to form a pseudo-fcc metal hydride with a slight tetragonal deformation (bct, $I4/mmm$) and hydrogen-to-metal ratio [H]/[M] = 2.5 [12, 15]. Such a high [H]/[M]-ratio has never been observed in pure transition metal hydrides and would mean that hydrogen occupies all tetrahedral and around half of the octahedral sites in the pseudo-fcc lattice. In transition metal hydrides, such as the binary hydrides TiH_2, ZrH_2 and PdH, the hydrogen atoms tend to occupy either the tetrahedral or octahedral interstices within the fcc lattice. It is not common that both the tetrahedral and octahedral sites are occupied at the same time. The sites occupied by hydrogen atoms are nearly always separated by at least 2.0-2.1 Å [20, 21] with very few exceptions [22]. This empirical rule is known as the *Switendick criterion* or the *2 Å rule*. In fcc hydrides the shortest distance between two adjacent sites is between one tetrahedral and one octahedral interstice $r_{t-o} = \sqrt{3/16} \cdot a_{\mathrm{fcc}}$. Thus, occupation of both tetrahedral and octahedral interstices requires a large unit cell with $a_{\mathrm{fcc}} \geq$ 4.62-4.85 Å. The reported lattice for $TiVZrNbHfH_{2.5}$ corresponds to a $a_{\mathrm{fcc}} \approx$ 4.5513(2) Å. Hence, it is possible that the Switendick criterion is violated in the case of $TiVZrNbHfH_{2.5}$ · It was suggested by Sahlberg et al. that "[...] the built in strain in an HEA could be the driving force to open up new interstitial sites for hydrogen". In this work we aim to investigate whether a similar effect can be observed in other HEAs with comparable local lattice strain. The HEAs TiVNbTa $(\delta r, \Omega) = (3.53\ \%, 388)$ and TiVZrNb $(\delta r, \Omega) = (6.03\ \%, 169)$ have been reported to assume single-phase bcc solid solutions in the as cast state [23, 24]. As the atomic radius of Zr is 1.60 Å, and the respective atomic radii of Ti, V, Nb and Ta are 1.46 Å, 1.35 Å, 1.47 Å and 1.47 Å [25], the local lattice strain can be tuned by altering the zirconium-to-metal ratio [Zr]/[M] in the HEA. Here, we chose the systems $TiVZr_zNbTa_{1-z}$ and $TiVZr_{1+z}Nb$ as our model systems.

Experimental details

Four samples of $\mathrm{TiVZr_zNbTa_{1\text{-}z}}$ with $z \in \{0, 0.15, 0.50, 0.74\}$ and five samples of $\mathrm{TiVZr_{1+z}Nb}$ with $z \in \{0, 0.20, 0.50, 0.75, 1.0\}$ were synthesized from lumps of Ti, Nb, Ta (Goodfellow, 99.99 % metals basis), V (Goodfellow, 99.6 % metals basis) and Zr (Alfa Aesar, 95.8 % metals basis) by arc melting under Ar atmosphere. Ti oxygen-getter pieces were melted initially and the samples were subsequently turned and remelted five times to enhance their homogeneity. The final compositions can be considered as very close to the nominal ones as the mass losses during arc-melting were less than 0.3 wt.%. The overall chemical composition of TiVNbTa, $\mathrm{TiVZr_{0.5}NbTa_{0.5}}$, TiVZrNb, $\mathrm{TiVZr_{1.5}Nb}$ and $\mathrm{TiVZr_2Nb}$ were also confirmed by energy dispersive X-ray spectrometry (EDS) analysis. Parts of the as cast samples were filed into coarse powders for phase identification using a metal file. The rest was cut into smaller pieces with a long handled bolt cutter. These pieces were subsequently loaded into an in-house built Sieverts apparatus [26] where they were exposed to an activation treatment by heating to 350 °C under dynamic vacuum for 1-2 hours. The samples were then cooled to room temperature and exposed to hydrogen gas at ~ 20 bar to obtain the corresponding metal hydrides. The absorption were in all cases complete within minutes, and the final pressures were typically 11-16 bar H_2. An additional batch of hydrides was synthesized from TiVNbTa, $\mathrm{TiVZr_{0.5}NbTa_{0.50}}$, TiVZrNb, $\mathrm{TiVZr_{1.5}Nb}$ and $\mathrm{TiVZr_2Nb}$ following the same route of synthesis as discussed above but with a hydrogen pressure of 80 bar. The samples were handled and stored inside an MBraun Unilab glovebox with purified Ar atmosphere (< 1 ppm O_2 and H_2O).

Both *ex situ* and *in situ* synchrotron radiation powder X-ray diffraction (SR-PXD) patterns were measured at the P02.1 beamline at PETRA-III at the German Electron Synchrotron (DESY) in Hamburg, Germany using a PerkinElmer XRD1621 detector with a sample-to-detector distance of 870 mm and a fixed wavelength of $\lambda = 0.2071$ Å. The exposure time was 20 s in the *ex situ* measurements while it was 10 s during the *in situ* measurements. *Ex situ* SR-PXD patterns were also measured at the Swiss-Norwegian beamlines (SNBL) at the European Synchrotron Radiation Facility (ESRF) in Grenoble, France using a Dectris Pilatus 2M detector [27] with sample-to-detector distance 147 mm, 10 s exposure time and $\lambda = 0.7896$ Å. The samples were contained in borosilicate glass and sapphire capillaries during the *ex situ* and *in situ* measurements respectively. The sapphire capillaries were connected to an in-house built Swagelok cell and placed under 1 bar of gaseous Ar. The temperature was controlled through ohmic heating in a kanthal wire that was tightly wrapped around the sapphire capillary. Laboratory PXD patterns were measured with a Bruker D8 Advance diffractometer with Cu-Kα radiation ($\lambda_{\mathrm{K}\alpha1} = 1.5406$ Å, $\lambda_{\mathrm{K}\alpha2} = 1.5444$ Å). Phase identification was performed by search-matches with the PDF-4 database and the EVA software. Further analysis was performed with the Rietveld method using GSAS-II [28]. In a typical refinement the background was accounted for by a 16$^{\mathrm{th}}$ order shifted Chebyschev polynomial. The peaks were modelled by a Thompson-Cox-Hastings pseudo-Voigt function [29] with 4 refineable parameters. The zero offset, displacement factors, lattice parameters and phase fractions were also refined.

The elemental composition was studied by EDS in a Zeiss Merlin scanning electron microscope (SEM) equipped with an X-Max 80 mm^2 Silicon Drift Detector. The data was acquired using an acceleration voltage of 20 kV and a beam current of 1 nA for 20 min at a working distance of 8.5 mm. The data was evaluated using the AZtec software. Prior to analysiss the samples were prepared by mechanical grinding using 220 grit SiC paper, followed by polishing using 9 μm, 3μm and 1μm diamond suspensions. Finally, the samples were polished using a H_2O_2:SiO_2 (1:5 ratio) mixture.

Thermogravimetric analysis (TGA) and differential scanning calorimetry (DSC) were measured simultaneously with a heat flux type Netzsch STA 449 F3 Jupiter apparatus. In a typical measurement a ~ 45 mg sample was placed inside an alumina crucible equipped with a pierced lid. The measurement was then conducted under flowing Ar at 50 mL/min. The samples were briefly exposed to air when they were loaded into the apparatus.

Results and discussion

Values for Ω and δr were calculated for all the investigated alloys using equation 1 and 2. In these calculations, values for r_i and T_m were taken from [25], ΔH_{mix} was calculated in the Miedema approximation [30] and ΔS_{mix} was estimated with the Boltzmann formula. Table 1 shows that these systems include a wide range of values of both δr and Ω. Notice that very high values for Ω occur when $\Delta H_{mix} \to 0$. Fig. 1 shows Rietveld refinements performed on a representative selection of the SR-PXD patterns of the as cast alloys and their corresponding hydrides. Excellent fits are obtained for the as cast alloys with a bcc single-phase ($Im\overline{3}m$). Fig. 2 show SEM and EDS mappings for as cast TiVNbTa, TiVZrNb and $TiVZr_2Nb$. It can be seen that the alloys have dendritic microstructures. In general, the microstructure of the as cast alloys get less dendritic with increasing [Zr]/[M]. The chemical compositions of the different regions were determined with EDS, and the results are shown in table 2. The average compositions of the investigated areas correspond to the nominal within the measurement uncertainties (±1-2 at.%). The only exception is that it seems to be less Nb than expected in TiVZrNb. A possible explanation is that some Nb is interpreted as Zr since these two elements have overlapping energies ($\mathrm{L}\alpha_{\mathrm{Zr}} = 2.042$ keV, $\mathrm{L}\alpha_{\mathrm{Nb}} = 2.166$ keV). For $\mathrm{TiVZr_2Nb}$ the variation in the chemical composition between the dendrite and interdendrite matrix is within the measurement uncertainty. The dendrites in TiVNbTa are significantly depleted in Ta when compared to the interdendrite matrix. The composition appears to change smoothly from the dendrite to the interdendrite matrix. In the case of TiVZrNb, the dendrites are enriched in Zr. However, table 2 shows that $(\delta r - \delta r_{nominal})/\delta r_{nominal}$ is less than 0.06 in the different regions. The local lattice strain for the nominal compositions shown in table 1 can therefore be considered as representative for the overall alloys. Similar SEM and EDS analyses for $\mathrm{TiVZr_{0.5}NbTa_{0.5}}$ and $\mathrm{TiVZr_{1.5}Nb}$ can be found in fig. A.1 and table A.1 in the supplementary information. The main phase of the hydrides synthesized at 20 bar $\mathrm{H_2}$ is fcc ($Fm\overline{3}m$). For the Ta-containing hydrides there is an additional phase present that is bct ($I4/mmm$) for $\mathrm{TiVNbTaH_x}$ (30.3 wt.%) and $\mathrm{TiVZr_{0.15}NbTa_{0.85}H_x}$ (24.2 wt.%), while it is bcc for $\mathrm{TiVZr_{0.5}NbTa_{0.5}H_x}$ (8.2 wt.%) and $\mathrm{TiVZr_{0.74}NbTa_{0.26}H_x}$ (2.2 wt.%). As Nb and Ta have significantly higher melting points than Ti, V and Zr, the additional phases could be hydrides formed from unmelted Nb or Ta. However, we find this unlikely since the lattice parameters of both Nb and Ta are significantly larger than in for example TiVNbTa with the largest amount of the additional phase. Thus, unmelted Nb or Ta should have been clearly visible in the SR-PXD patterns in fig. 1, but this is not the case. Müller et al. [31] observed that a bct/fcc or bcc/fcc two-phase region was obtained for a broad range of compositions for $Ta_zV_{1-z}H_x$. A similar reaction could have taken place in our samples.

The bcc and fcc lattice parameters for the considered systems are shown in table 1. No significant differences could be observed by PXD, TG/DSC or manometric measurements between the hydrides synthesized at 80 bar H_2 and those synthesized at 20 bar H_2. Therefore, the hydrides synthesized at 80 bar H_2 will not be discussed further. Fig. 3 shows that both the bcc and fcc unit cells expand linearly when [Zr]/[M] increases. This is expected as the atomic radius of Zr is significantly larger than the radii of the other elements.

The minimum for a_{fcc} that allow simultaneous occupation of both tetrahedral and octahedral interstices without violating the Switendick criterion is shown in fig. 3. From the figure, it is clear that the lattice parameters of the investigated hydrides are too small to expect the hydrogen atoms to occupy both the tetrahedral and octahedral sites in accordance with the *2 Å rule*. However, such an analysis is based on the average structure. In HEAs with large local lattice strain the distance between the tetrahedral and octahedral lattice sites will deviate locally from the average. Thus, a fraction of the octahedral sites may be sufficiently displaced from the neighbouring tetrahedral sites to become available for hydrogen occupation. It is also possible that the lattice would expand sufficiently to allow simultaneous occupation of

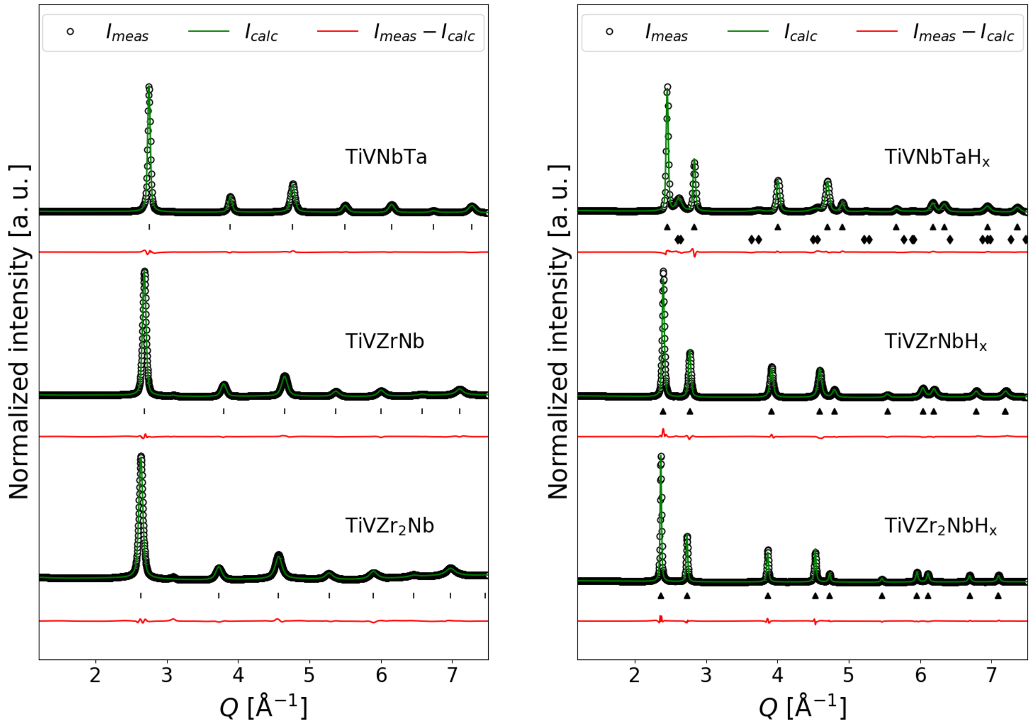

Fig. 1: Selected Rietveld refinements from the SR-PXD patterns of the as cast HEA alloys (right) and their corresponding hydrides (left). The peaks belonging to bcc ($Im\bar{3}m$), fcc ($Fm\bar{3}m$) and bct ($I4/mmm$) phases are indicated by |, ▲ and ♦, respectively.

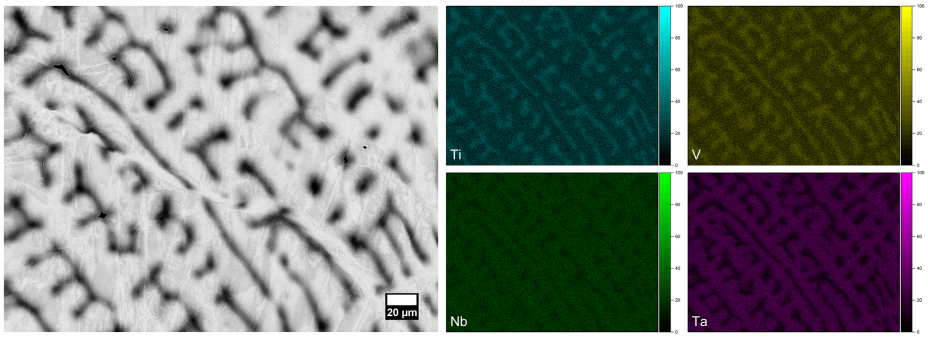

(a) TiVNbTa

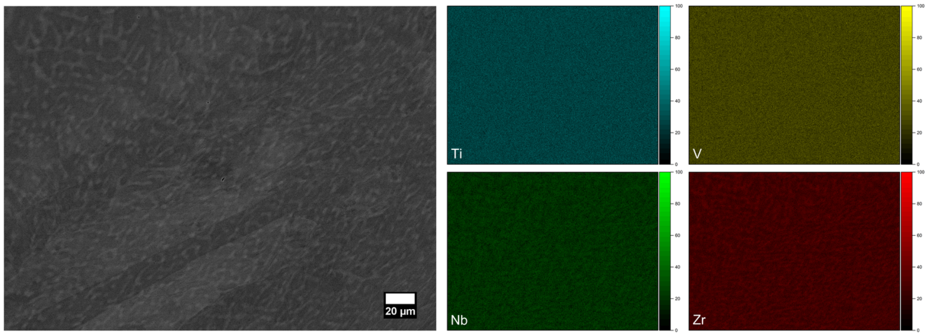

(b) TiVZrNb

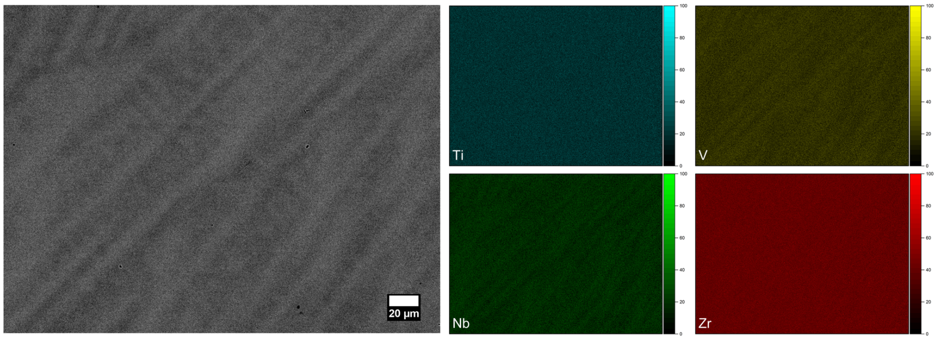

(c) TiVZr$_2$Nb

Fig. 2: Backscattered electron images (left) and EDS maps (right) of **(a)** as cast TiVNbTa, **(b)** as cast TiVZrNb and **(c)** as cast TiVZr$_2$Nb.

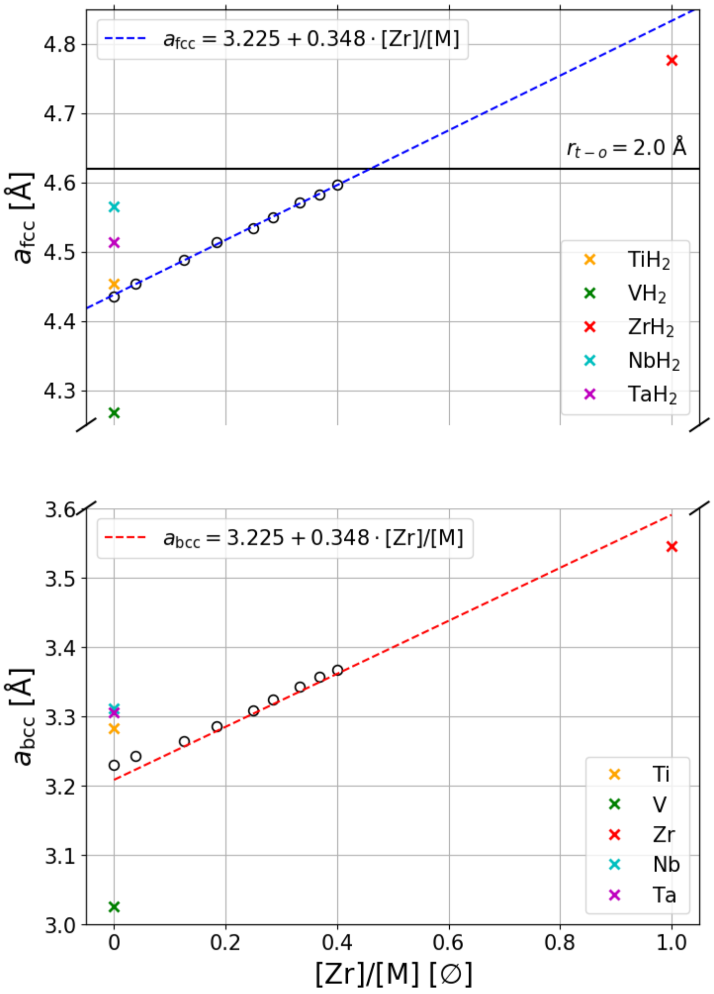

Fig. 3: The lattice parameters obtained from Rietveld refinements, a_{bcc} and a_{fcc}, of the bcc alloys and the fcc hydrides as a function of the [Zr]/[M]. The error bars are within the data points. The compositions corresponding to the respective data points can be determined from table 1. The dashed lines are linear regressions. The solid black line in the upper panel indicate the critical value for a_{fcc} where the distance between the octahedral and tetrahedral sites in the fcc matrix, r_{t-o}, is equal to 2.0 Å. The lattice parameters of the bcc allotrope of the raw materials [32–36] are shown for comparison in the lower part of the figure, while the fcc allotrope of the corresponding binary hydrides [31, 37–39] are shown in the upper part.

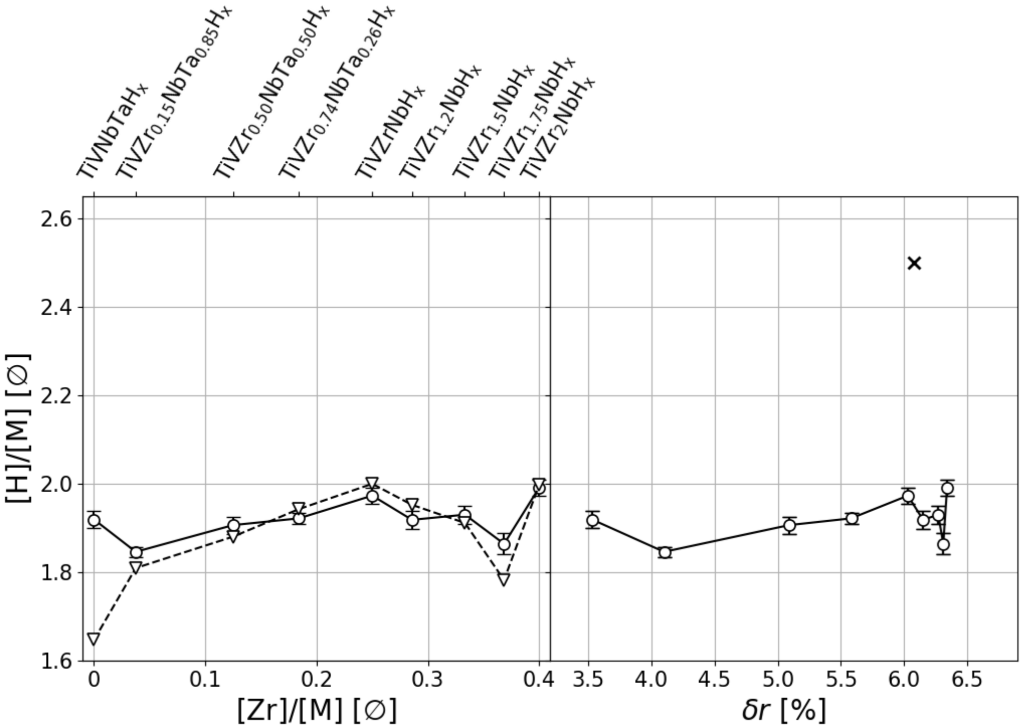

Fig. 4: Manometric (○) and gravimetric (▽) measurements of the [H]/[M]-ratios of the samples as a function of their [Zr]/[M] and the HEA parameter δr as defined in equation 2. The corresponding value for the TiVZrNbHf (×) that was reported by Sahlberg et al. [12] are shown for comparison. As the local lattice strain δr increases with [Zr]/[M], the order of the compounds is the same in both figures.

Table 1: Comparison of the zirconium-to-metal ratio [Zr]/[M], local lattice strain δr, the Ω HEA parameter, the bcc lattice parameter a_{bcc} and fcc lattice parameter a_{fcc} for the considered systems.

System	[Zr]/[M] [∅]	δr [%]	Ω [∅]	a_{bcc} [Å]	a_{fcc} [Å]
TiVNbTa	0	3.53	388	3.2295(2)	4.4355(4)
$\mathrm{TiVZr_{0.15}NbTa_{0.15}}$	0.04	4.10	455941	3.2419(1)	4.4544(2)
$\mathrm{TiVZr_{0.50}NbTa_{0.50}}$	0.13	5.09	551	3.2638(3)	4.4889(3)
$\mathrm{TiVZr_{0.74}NbTa_{0.26}}$	0.18	5.58	701370	3.2852(3)	4.5132(2)
TiVZrNb	1.00	6.03	169	3.3076(2)	4.5336(2)
$\mathrm{TiVZr_{1.20}Nb}$	0.29	6.15	191	3.3234(3)	4.5499(1)
$\mathrm{TiVZr_{1.50}Nb}$	0.33	6.27	228	3.3418(3)	4.5706(1)
$\mathrm{TiVZr_{1.75}Nb}$	0.37	6.31	260	3.3571(3)	4.5827(1)
$\mathrm{TiVZr_2Nb}$	0.40	6.34	296	3.3674(3)	4.5968(1)

tetrahedral and octahedral interstices when the alloy is heated or if [Zr]/[M] is increased further.

The manometric and gravimetric measurements of the hydrogen content in our HEAs are shown in fig. 4. The [H]/[M]-ratios are close to, but never exceed, 2. This indicates that the hydrogen atoms occupies the tetrahedral sites in the fcc hydrides. There are no trends in the [H]/[M]-ratios in relation to the HEA parameter δr nor the zirconium-to-metal-ratio [Zr]/[M]. This is interesting as the five systems that contain the highest amounts of Zr, $\mathrm{TiVZr_{1+z}Nb}$ z $\in \{0, 0.2, 0.5, 0.75, 1\}$ have comparable local lattice strain δr to TiVZrNbHf [12]. Thus, the large [H]/[M]-ratio that was reported for this system can not be explained by the large local lattice strain alone. It is

Table 2: The compositions of TiVNbTa, TiVZrNb and $TiVZr_2Nb$ measured by EDS. δr values were calculated as described earlier.

Composition	Elements					δr [%]
	Ti	V	Zr	Nb	Ta	
TiVNbTa (nominal)	0.25	0.25	0	0.25	0.25	3.53
TiVNbTa (average)	0.26	0.26	0	0.23	0.25	3.57
TiVNbTa (dendrite)	0.32	0.31	0	0.21	0.17	3.76
TiVNbTa (interdendrite)	0.23	0.23	0	0.25	0.29	3.44
TiVZrNb (nominal)	0.25	0.25	0.25	0.25	0	6.03
TiVZrNb (average)	0.27	0.27	0.26	0.20	0	6.22
TiVZrNb (dendrite)	0.27	0.27	0.30	0.18	0	6.37
TiVZrNb (interdendrite)	0.27	0.28	0.24	0.21	0	6.13
$TiVZr_2Nb$ (nominal)	0.20	0.20	0.40	0.20	0	6.34
$TiVZr_2Nb$ (average)	0.21	0.21	0.41	0.18	0	6.46
$TiVZr_2Nb$ (dendrite)	0.21	0.20	0.41	0.18	0	6.37
$TiVZr_2Nb$ (interdendrite)	0.21	0.22	0.41	0.17	0	6.54

reassuring that the manometric and gravimetric measurements in fig. 4 tend to agree within a few standard deviations. The only exception is $TiVNbTaH_x$ for which the manometric measurement exceeds the gravimetric value significantly. This might be due to outgassing of hydrogen during transport from the high-pressure environment inside the Sieverts apparatus to the TG/DSC. This is in agreement with the fact that the hydrides are destabilized when [Zr]/[M] decreases. Fig. 5 shows three representative TG/DSC measurements conducted during desorption of hydrogen from the hydrides. It can be seen that the desorption of hydrogen from the Zr-free $\mathrm{TiVNbTaH_x}$ is complete at ~ 500 °C, while ~ 900 °C is necessary to completely desorb the hydrogen from the most Zr-rich system, $\mathrm{TiVZr_2NbH_x}$.

As [Zr]/[M] increases, it is also evident from fig. 5 that the desorption process becomes more complex. For $\mathrm{TiVNbTaH_x}$ the desorption is composed of three steps. The first event with onset at 112 °C is endothermic and correlates to a mass loss of 0.2 wt.%. The second event with onset at 225 °C is also endothermic and is accompanied by the bulk mass loss. After this event the mass loss continue, although more slowly, and it is associated with a broad endothermic event. The first event is only observed for the Zr-free sample. Based upon similar measurements conducted for the other hydrides (see figure A.2 in the supplementary information), it is clear that when the zirconium-to-metal ratio increases above 25 at.% the second event splits into three. The desorption furthermore proceed in a more complex fashion past the original third event. For $\mathrm{TiVZr_2NbH_x}$ there is for instance an exothermic event at ~ 530 °C and two endothermic events at ~ 685 °C and ~ 792 °C, respectively. The endothermic events are associated with mass losses and are therefore due to hydrogen desorption. The exothermic event is on the other hand not associated with a mass loss, and might for instance indicate a structural transition. A similar exothermic event occur at about the same temperature when $[\mathrm{Zr}]/[\mathrm{M}] \geq 18.4$ at.%. This can be seen in fig. 5 for $\mathrm{TiVZrNbH_x}$ for which it occur at a slightly lower temperature.

To investigate whether the exothermic event is due to structural changes, laboratory PXD patterns of the desorbed hydrides were measured after TG/DSC. The PXD patterns are shown in fig. 6 from which it is evident that the bcc

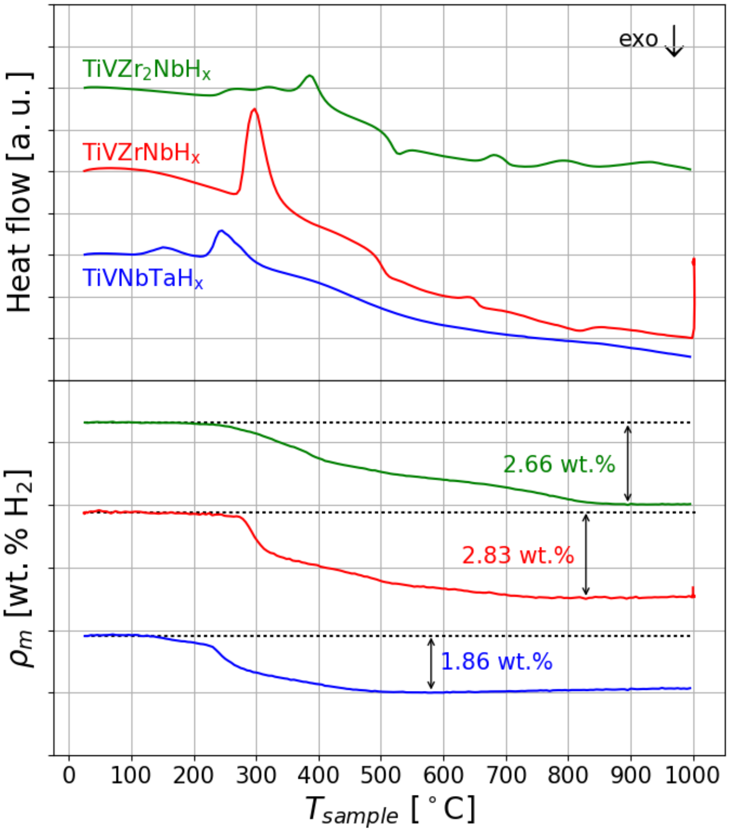

Fig. 5: TG/DSC measurements during hydrogen desorption from TiVNbTaH$_x$, TiVZrNbH$_x$ and TiVZr$_2$NbH$_x$. The upper part of the figure show the DSC heat flows while the corresponding mass loss ρ_m that is assumed to be solely due to desorption of hydrogen is shown in the lower part.

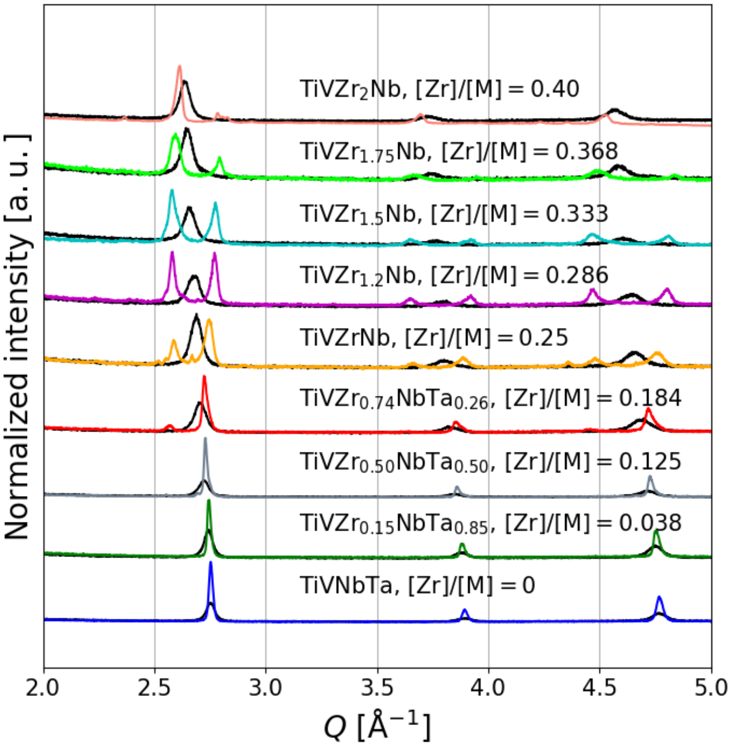

Fig. 6: Cu-Kα PXD patterns of the as cast alloys $\mathrm{TiVZr_zNbTa_{1\text{-}z}}$ and $\mathrm{TiVZr_{1+z}Nb}$ (black) and the alloys obtained after desorbing the hydrides at 1000 °C in the TG/DSC (colored).

HEA phase is retrieved when [Zr]/[M] < 0.125 corresponding to $\mathrm{TiVZr_{0.5}NbTa_{0.5}}$. For higher [Zr]/[M], we observe a phase separation in which the original bcc phase is split into two bcc phases whose peaks are positioned at either side of the original ones. The lattice parameters of the two bcc phases are shown in fig. 7 as a function of the zirconium-to-metal ratio. It is also clear from fig. 6 that the relative intensities of these phases change with [Zr]/[M]. The intensity of the bcc phase with the largest unit cell (i.e. at lowest scattering angle) increases with [Zr]/[M] when compared to that of the smallest. This indicates that the largest bcc phase is Zr-rich. Senkov et al. [24] have reported that no phase separation was observed when the bcc TiVZrNb HEA was annealed at 1200 °C for 24 hours. This indicates that the observed phase separation is induced when the hydrogen accommodated within the structure is desorbed, and not by the high temperature as such.

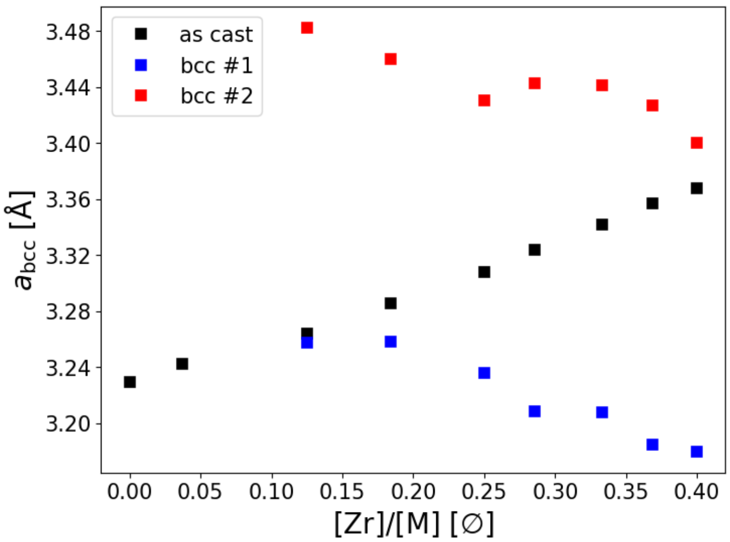

Fig. 7: The lattice parameters of the as cast alloys $\mathrm{TiVZr_zNbTa_{1\text{-}z}}$ ($[\mathrm{Zr}]/[\mathrm{M}] \in [0, 0.25]$) and $\mathrm{TiVZr_{1+z}Nb}$ ($[\mathrm{Zr}]/[\mathrm{M}] \in [0.25, 0.40]$) (black), and the two bcc phases observed after desorption at 1000 °C in the TG/DSC (coloured). The error bars are within the data points.

To investigate the phase separation we have followed the hydrogen desorption processes by *in situ* SR-PXD. The SR-PXD patterns that were measured during desorption of hydrogen from $\mathrm{TiVNbTaH_x}$, $\mathrm{TiVZr_{0.5}NbTa_{0.50}H_x}$, $\mathrm{TiVZrNbH_x}$ and $\mathrm{TiVZr_2NbH_x}$ are shown in fig. 8. These data are presented alongside the corresponding TG/DSC results and the phase fractions that were obtained from the sequential Rietveld refinements. The phase fractions are only reported up until the phase separation. This is because it is difficult to distinguish Ti from V and Zr from Nb because of their similar X-rays scattering. Thus, it is impossible to determine the exact compositions of the formed phases which is necessary to calculate the phase-fractions. However, all the observed peaks can be indexed, and reasonable fits can be achieved if the occupancy of Ti/V and Zr/Nb is refined. The results of the Rietveld refinements are shown in fig. A.3-A.6 in the supplementary information.

Fig. 8 shows that complete desorption of hydrogen was not achieved during the *in situ* SR-PXD measurements. This is especially clear in fig. 8 (c) and (d) where we are unable to obtain the two hydrogen-free bcc phases presented in fig. 6. A possible explanation is that the measurements were performed in a closed system that enable a partial pressure of $\mathrm{H_2}$ to build up during the desorption. Thus, the conditions are not identical to those in the TG/DSC measurements where the desorbed $\mathrm{H_2}$ is flushed away with the flowing Ar.

$TiVNbTaH_x$. As presented above there are three events in the desorption process when [Zr]/[M] = 0. Fig. 8 (a) shows that the first endothermic event with onset at 112 °C in the TG/DSC data correlates well to the transition from bct to bcc in the minority phase. The bulk mass loss in the second

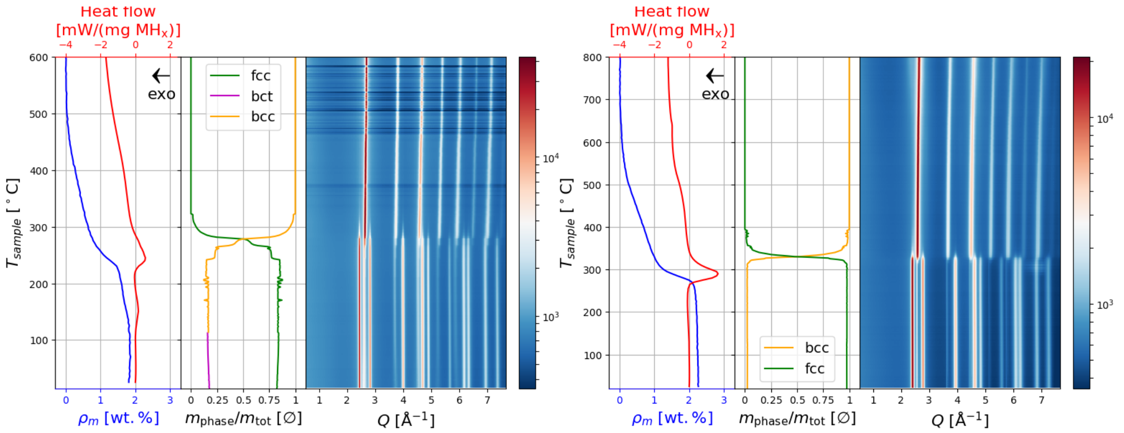

(a) $\mathrm{TiVNbTaH_x}$ **(b)** $\mathrm{TiVZr_{0.5}NbTa_{0.5}H_x}$

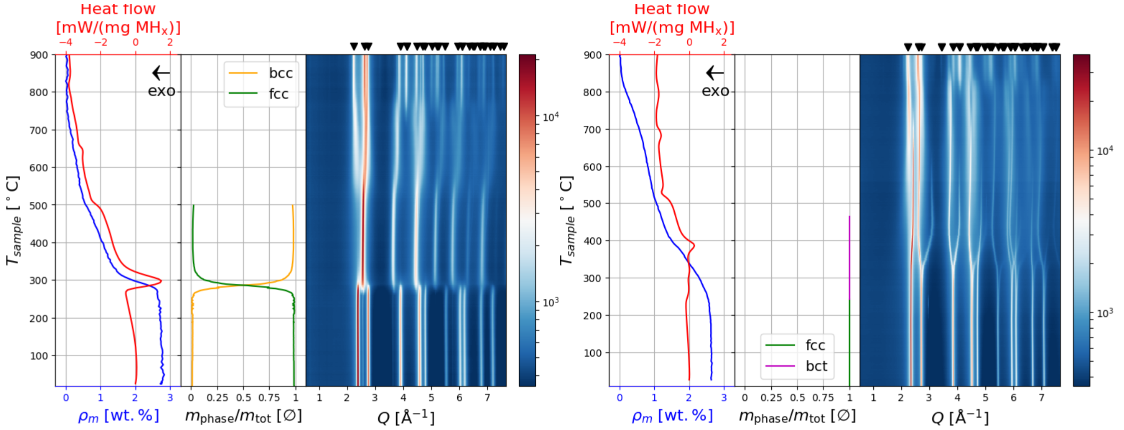

(c) $\mathrm{TiVZrNbH_x}$ **(d)** $\mathrm{TiVZr_2NbH_x}$

Fig. 8: *In situ* SR-PXD measurements during desorption of hydrogen from **(a)** $\mathrm{TiVNbTaH_x}$, **(b)** $\mathrm{TiVZr_{0.5}NbTa_{0.5}H_x}$, **(c)** $\mathrm{TiVZrNbH_x}$ and **(d)** $\mathrm{TiVZr_2NbH_x}$ alongside corresponding TG/DSC measurements and sequential refinement results. Peaks from a C15-type Laves phase ($Fd\bar{3}m$) are indicated by ▼. The heating rate were in all cases 10 °C/min.

endothermic event correlates similarly well to the transition from fcc to bcc in the main phase. Finally there is a slow, continuous mass loss from ~ 315 °C towards the end of the measurement that is associated with a contraction in the bcc phase. The contraction can be observed as shifts in the peaks to higher scattering angles. Fig. A.3 shows very good fits in the refinements.

$TiVZr_{0.5}NbTa_{0.5}H_x$. When the zirconium-to-metal ratio [Zr]/[M] is increased to 12.5 at.% (fig. 8 (b)), we observe a fcc phase alongside a minor bcc impurity phase initially. At 310 °C the fcc main phase transforms to a bcc phase. The compound now appears to be single phase bcc. As before, this phase contracts towards the end of the measurement indicating that the hydrogen desorption continue. At the highest temperatures, a shoulder appear on the low-angle side of the 110 bcc peak, but as no other peaks can be resolved for this phase its nature remains uncertain. It should be noted that the phase transition in the *in situ* SR-PXD data occurs at a slightly higher temperature than the endothermic event associated with the bulk mass loss in the TG/DSC data. This might be due to already discussed pressure differences between the TG/DSC and SR-PXD measurements. The obtained Rietveld fits from the refinements are very good (see fig. A.4). However, it should be noted that the refinement is slightly poorer in the temperature regime around the phase transition. This is probably due to rapid reaction rate and limited time resolution.

$TiVZrNbH_x$. When [Zr]/[M] reaches 25 at.% (fig. 8 (c)), the fcc hydride transforms to a bcc hydride at 275 °C. As before the bcc unit cell contracts after the phase transition, and again a shoulder appear at 500 °C on the low-angle side of the 110 bcc peak. However, this time the shoulder grows into a new phase with broad peaks that can be indexed as fcc. The onset of the exothermic event at 480 °C in the TG/DSC data correlates reasonably well this phase-separation. The new fcc phase becomes more resolved until 700 °C where part of it transforms to a C15-type Laves phase ($Fd\overline{3}m$), isostructural to $\mathrm{ZrV_2D_x}$ [40]. The desorption is then unable to commence any further, but we expect that the C15 Laves phase eventually would transfer into the larger bcc phase presented in fig. 6 if hydrogen was removed from the capillary. The peaks corresponding to the smaller bcc phase would then correspond to the bcc phase observed towards the end of the measurement in figure 8c. Selected Rietveld refinements are shown in fig. A.5. Again, the refinements are slightly poorer in the temperature regime around transitions.

TiVZr₂NbH$_x$. When [Zr]/[M] reaches 40 at.% (fig. 8 (d)), the fcc hydride transforms to a bct hydride ($I4/mmm$) at 253 °C. When the temperature reaches 530 °C, the fcc phase appears on the low-angle side of the 101 bct peak. This event correlates well to the exothermic event that is observed in the TG/DSC measurement. When the temperature reaches 749 °C the bct phase has turned into a bcc phase, but the intensity of this phase is much lower than for $\mathrm{TiVZrNbH_x}$. At 794 °C part of the new fcc phase is transformed to a C15-type Laves phase. This is similar to what was observed for $\mathrm{TiVZrNbH_x}$, however for $\mathrm{TiVZr_2NbH_x}$ there are eventually no distinguishable peaks from the bcc phase which dominated the diffraction patterns towards the end of the *in situ* measurement for $\mathrm{TiVZrNbH_x}$, see fig. 8 (c). This fits well with our hypothesis that that the C15 Laves phase eventually turns into the larger bcc phase shown in fig. 6 as this is the main phase of the desorbed $\mathrm{TiVZr_2Nb}$ and only a minority phase for desorbed TiVZrNb after TG/DSC. Selected Rietveld refinements are shown in fig. A.6.

Conclusion

Four samples of $\mathrm{TiVZr_zNbTa_{1\text{-}z}}$ with $z \in \{0, 0.15, 0.50, 0.74\}$ and five samples of $\mathrm{TiVZr_{1+z}Nb}$ with $z \in \{0, 0.20, 0.50, 0.75, 1.0\}$ were successfully synthesised by arc melting, and their corresponding hydrides were synthesized by hydrogenation in a Sieverts apparatus. SEM and EDS mappings reveal that the microstructure of the as cast alloys get less dendritic with increasing [Zr]/[M]. There are some variation in the chemical composition between the dendrite and interdendrite matrix in the alloys with the most dendritic microstructures. However, the variation in local lattice strain from the nominal, $(\delta r - \delta r_{nominal})/\delta r_{nominal}$, is in all cases less than 0.06. The crystalline phases were determined by SR-PXD. The alloys have bcc ($Im\overline{3}m$) crystal structures and form fcc ($Fm\overline{3}m$) hydrides with [H]/[M] close to but never exceeding 2. No correlation between the [H]/[M] and the lattice strain δr is observed in this work. Both bcc and fcc unit cells expand linearly when the zirconium-to-metal ratio [Zr]/[M] increases. TG/DSC indicate that the stability of the hydrides increases with [Zr]/[M]. When heated, the hydrides decompose into the original bcc alloys if $[\mathrm{Zr}]/[\mathrm{M}] < 12.5$ at.%. If $[\mathrm{Zr}]/[\mathrm{M}] \geq 12.5$ at.%, the hydrides phase-separate in a hydrogen induced decomposition type process. The result is then a combination of two bcc phases, one with a larger unit cell and another with a smaller unit cell than that of the original bcc alloy. The amount of the phase with the largest unit cell increases with [Zr]/[M]. The phase-seperation was further investigated with *in situ* SR-PXD. The phase-separation correlates with an exothermic event that was observed by

TG/DSC at 530 °C. At this temperature, a strained fcc phase appear in the *in situ* SR-PXD measurements. It is eventually transformed into a C15-type Laves phase ($Fd\bar{3}m$). The experimental conditions prevent full dehydrogenation, but we expect that the C15-type Laves phase eventually transform to the bcc phase with largest unit cell.

Acknowledgements

This work is funded by the NordForsk Nordic Neutron Science Programme through the functional hydrides (FunHy) project (grant number 81942). The skilful assistance of the staff at both the Swiss-Norwegian beamline at the European Synchrotron Radiation Facility in Grenoble, France and the P02.1 beamline at the German Electron Synchrotron in Hamburg, Germany is greatly acknowledged. Torben René Jensen, Aarhus University is acknowledged for allowing us to use their hydrogen gas rig during the *in situ* SR-PXD measurements.

Dennis Karlsson acknowledge support from the Swedish Foundation for Strategic Research through the SSF - Development of processes and Materials in the AM project.

Appendix A. Supplementary data

Supplementary data to this article can be found online at ... .

References

[1] Y. Ye, Q. Wang, J. Lu, C. Liu, Y. Yang, High-entropy alloy: challenges and prospects, Materials Today 19 (2016) 349–362.

[2] X. Yang, Y. Zhang, Prediction of high-entropy stabilized solid-solution in multi-component alloys, Materials Chemistry and Physics 132 (2012) 233–238.

[3] D. Miracle, O. Senkov, A critical review of high entropy alloys and related concepts, Acta Materialia 122 (2017) 448–511.

[4] G. Walker, Solid-state hydrogen storage: materials and chemistry, Elsevier, 2008.

[5] A. Züttel, Materials for hydrogen storage, Materials today 6 (2003) 24–33.

[6] M. Bououdina, D. Grant, G. Walker, Review on hydrogen absorbing materialsstructure, microstructure, and thermodynamic properties, International Journal of Hydrogen Energy 31 (2006) 177–182.

[7] P. Chen, M. Zhu, Recent progress in hydrogen storage, Materials today 11 (2008) 36–43.

[8] F. Zhang, P. Zhao, M. Niu, J. Maddy, The survey of key technologies in hydrogen energy storage, International Journal of Hydrogen Energy 41 (2016) 14535–14552.

[9] Y.-F. Kao, S.-K. Chen, J.-H. Sheu, J.-T. Lin, W.-E. Lin, J.-W. Yeh, S.-J. Lin, T.-H. Liou, C.-W. Wang, Hydrogen storage properties of multi-principal-component CoFeMnTixVyZrz alloys, International Journal of Hydrogen Energy 35 (2010) 9046–9059.

[10] I. Kunce, M. Polanski, J. Bystrzycki, Structure and hydrogen storage properties of a high entropy ZrTiVCrFeNi alloy synthesized using laser engineered net shaping (LENS), International Journal of Hydrogen Energy 38 (2013) 12180–12189.

[11] I. Kunce, M. Polanski, J. Bystrzycki, Microstructure and hydrogen storage properties of a TiZrNbMoV high entropy alloy synthesized using laser engineered net shaping (LENS), International Journal of Hydrogen Energy 39 (2014) 9904–9910.

[12] M. Sahlberg, D. Karlsson, C. Zlotea, U. Jansson, Superior hydrogen storage in high entropy alloys, Scientific Reports 6 (2016).

[13] I. Kunce, M. Polański, T. Czujko, Microstructures and hydrogen storage properties of LaNiFeVMn alloys, International Journal of Hydrogen Energy 42 (2017) 27154–27164.

[14] S.-K. Chen, P.-H. Lee, H. Lee, H.-T. Su, Hydrogen storage of C14-CruFevMnwTixVyZrz alloys, Materials Chemistry and Physics 210 (2018) 336–347.

[15] D. Karlsson, G. Ek, J. Cedervall, C. Zlotea, K. T. Møller, T. C. Hansen, J. Bednarcik, M. Paskevicius, M. H. Sørby, T. R. Jensen, U. Jansson, M. Sahlberg, Structure and hydrogenation properties of a HfNbTiVZr high-entropy alloy, Inorganic Chemistry 57 (2018) 2103–2110.

[16] G. Zepon, D. Leiva, R. Strozi, A. Bedoch, S. Figueroa, T. Ishikawa, W. Botta, Hydrogen-induced phase transition of MgZrTiFe 0.5 Co 0.5

Ni 0.5 high entropy alloy, International Journal of Hydrogen Energy 43 (2018) 1702–1708.

[17] C. Zlotea, M. Sow, G. Ek, J.-P. Couzinié, L. Perrière, I. Guillot, J. Bourgon, K. Møller, T. Jensen, E. Akiba, M. Sahlberg, Hydrogen sorption in TiZrNbHfTa high entropy alloy, Journal of Alloys and Compounds 775 (2018) 667–674.

[18] C. Zhang, Y. Wu, L. You, X. Cao, Z. Lu, X. Song, Investigation on the activation mechanism of hydrogen absorption in TiZrNbTa high entropy alloy, Journal of Alloys and Compounds 781 (2018) 613–620.

[19] H. Shen, J. Zhang, J. Hu, J. Zhang, Y. Mao, H. Xiao, X. Zhou, X. Zu, A novel TiZrHfMoNb high-entropy alloy for solar thermal energy storage, Nanomaterials 9 (2019) 248.

[20] A. Switendick, Band structure calculations for metal hydrogen systems, Zeitschrift für Physikalische Chemie, Neue Folge 117 (1979) 89.

[21] B. Rao, P. Jena, Switendick criterion for stable hydrides, Physical Review B 31 (1985) 6726.

[22] V. Yartys, R. Denys, B. Hauback, H. Fjellvåg, I. Bulyk, A. Riabov, Y. M. Kalychak, Short hydrogen–hydrogen separations in novel intermetallic hydrides, RE3Ni3In3D4 (RE= La, Ce and Nd), Journal of Alloys and Compounds 330 (2002) 132–140.

[23] X. Yang, Y. Zhang, P. Liaw, Microstructure and compressive properties of NbTiVTaAlx high entropy alloys, Procedia Engineering 36 (2012) 292–298.

[24] O. Senkov, S. Senkova, C. Woodward, D. Miracle, Low-density, refractory multi-principal element alloys of the Cr–Nb–Ti–V–Zr system: Microstructure and phase analysis, Acta Materialia 61 (2013) 1545–1557.

[25] C. Kittel, P. McEuen, P. McEuen, Introduction to solid state physics, volume 8, Wiley New York, 1996.

[26] H. Brinks, A. Fossdal, R. Bowman, B. Hauback, Pressure–composition isotherms of TbNiAlH x, Journal of Alloys and Compounds 417 (2006) 92–95.

[27] V. Dyadkin, P. Pattison, V. Dmitriev, D. Chernyshov, A new multipurpose diffractometer PILATUS @ SNBL, Journal of Synchrotron Radiation 23 (2016).

[28] B. H. Toby, R. B. Von Dreele, GSAS-II: the genesis of a modern open-source all purpose crystallography software package, Journal of Applied Crystallography 46 (2013) 544–549.

[29] P. Thompson, D. Cox, J. Hastings, Rietveld refinement of Debye–Scherrer synchrotron X-ray data from Al2O3, Journal of Applied Crystallography 20 (1987) 79–83.

[30] A. Debski, R. Debski, W. Gasior, New features of entall database: comparison of experimental and model formation enthalpies, Archives of Metallurgy and Materials 59 (2014) 1337–1343.

[31] H. Müller, K. Weymann, Investigation of the ternary systems Nb-VH and Ta-VH, Journal of the Less Common Metals 119 (1986) 115–126.

[32] B. Levinger, Lattice parameter of beta titanium at room temperature, JOM 5 (1953) 195–195.

[33] O. Carlson, C. Owen, Preparation of high-purity vanadium metal by the iodide refining process, Journal of the Electrochemical Society 108 (1961) 88–93.

[34] R. Russell, Coefficients of thermal expansion for zirconium, JOM 6 (1954) 1045–1052.

[35] A. Seybolt, Solid solubility of oxygen in columbium, JOM 6 (1954) 774–776.

[36] G. Brauer, K. H. Zapp, Die nitride des tantals, Zeitschrift für anorganische und allgemeine Chemie 277 (1954) 129–139.

[37] H. Yakel, Thermocrystallography of higher hydrides of titanium and zirconium, Acta Crystallographica 11 (1958) 46–51.

[38] B. Nowak, Nuclear magnetic resonance study of the dihydride phase of the Ti-VH system, Journal of the Less Common Metals 101 (1984) 245–258.

[39] R. Beck, Zirconium-hydrogen phase system, American Society for Metals, Transactions Quarterly 55 (1962) 542.

[40] J.-J. Didisheim, K. Yvon, P. Fischer, P. Tissot, Order-disorder phase transition in ZrV2D3. 6, Solid State Communications 38 (1981) 637–641.